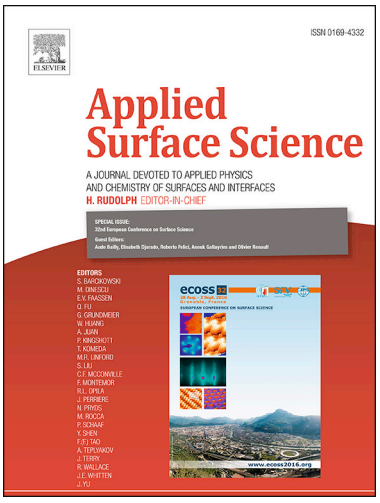

Full Length Article

A Promising Orthopedic Implant Material with Enhanced Osteogenic and Antibacterial Activity: Al_2O_3-coated Aluminum Alloy

Yuchang Weng, Hanxia Liu, Shunping Ji, Qian Huang, Hao Wu, Zhibin Li, Zhongzhen Wu, Huaiyu Wang, Liping Tong, Ricky K.Y. Fu, Paul K. Chu, Feng Pan

PII: S0169-4332(18)31800-2
DOI: https://doi.org/10.1016/j.apsusc.2018.06.233
Reference: APSUSC 39741

To appear in: *Applied Surface Science*

Received Date: 20 March 2018
Revised Date: 31 May 2018
Accepted Date: 25 June 2018

Please cite this article as: Y. Weng, H. Liu, S. Ji, Q. Huang, H. Wu, Z. Li, Z. Wu, H. Wang, L. Tong, R.K.Y. Fu, P.K. Chu, F. Pan, A Promising Orthopedic Implant Material with Enhanced Osteogenic and Antibacterial Activity: Al_2O_3-coated Aluminum Alloy, *Applied Surface Science* (2018), doi: https://doi.org/10.1016/j.apsusc.2018.06.233

A Promising Orthopedic Implant Material with Enhanced Osteogenic and Antibacterial Activity: Al_2O_3-coated Aluminum Alloy

Yuchang Weng [a,1], Hanxia Liu [b,1], Shunping Ji [a], Qian Huang [a], Hao Wu [a], Zhibin Li [b,c], Zhongzhen Wu [a,c *], Huaiyu Wang [b,*], Liping Tong [b], Ricky K. Y. Fu [c], Paul K. Chu [c,*], Feng Pan [a]

[a] School of Advanced Materials, Peking University Shenzhen Graduate School, Shenzhen 518055, China

[b] Institute of Biomedicine and Biotechnology, Shenzhen Institutes of Advanced Technology, Chinese Academy of Sciences, Shenzhen, 518055, China.

[c] Department of Physics and Department of Materials Science and Engineering, City University of Hong Kong, Tat Chee Avenue, Kowloon, Hong Kong, China

[*] Corresponding author. Tel/Fax: 86-755-26614661.
E-mail address: wuzz@pkusz.edu.cn (Z. Z. Wu), hy.wang1@siat.ac.cn (H. Y. Wang), paul.chu@cityu.edu.hk (P. K. Chu).

Abstract

Better orthopedic implants improve the life quality of patients and elderly people. Compared to Ti and Mg alloys commonly found in bone implants, Al alloys have merits such as high specific strength, excellent casting capability, and low cost, but unfortunately, the poor wear resistance, corrosion resistance, and insufficient biocompatibility have hampered wider application to bone replacements. In this study, well structure designed and excellent adhered Al_2O_3 coating is fabricated by micro-arc oxidation (MAO) on Al alloys to improve the wear resistance and corrosion resistance and inhibit release of potentially harmful Al ions from the Al alloy substrate. Ca, Fe, and Zn are respectively doped into the Al_2O_3 coating to enhance the biological properties. In particular, the Al_2O_3 coating doped with Zn delivers outstanding osteogenic performance and the antibacterial rates against *E. coli* and *S. aureus* are 99.5±0.56% and 98.77±0.52%, respectively. The improved mechanical and biological properties reveals that the Al_2O_3 coated Al alloys prepared by MAO coatings have large potential in orthopedic applications.

Keywords

Al_2O_3 coating; Al alloy; micro-arc oxidation; element doping; biological properties

1. Introduction

Osteoporosis, a senile disease, is becoming more prevalent as baby boomers age [1], thus, artificial implants are often needed. Most orthopedic implants are made of titanium (Ti) alloys with high strength, good corrosion resistance, and moderate biocompatibility [2-4]. Nevertheless, the elastic modulus of Ti-based implants is larger than that of natural bones which will cause potential resorption of tissues adjacent to the implants due to the stress shielding effect. Although biodegradable magnesium (Mg) alloys have merits such as the light weight, good biodegradability, and similar elastic modulus compared to human bone which make them promising for orthopedic applications [5-7], Mg-based implants may not have the proper corrosion resistance and mechanical properties under weight-bearing conditions.

As a common-used light alloy, aluminum (Al) alloys are similar to Mg alloys in terms of weight and elastic modulus and have comparable yield strength as Ti alloys, which makes them potential candidates of orthopedic implant materials. In addition, aluminum alloys also possess favorable properties such as good casting ability and low price, which can remarkably reduce the economic cost of manufacturing and using of implant materials. Nonetheless, potentially toxic Al ions can be released and cause biocompatibility problems. Besides, owing to their relatively poor anti-corrosion characteristics and large intrinsic friction coefficient, Al alloys can easily be worn and eroded during using. Hence, Al alloys have barely been used as orthopedic implants. However, if appropriately protective surface modification can be implemented on Al alloys, it is possible to carry forward their good mechanical

properties and to mitigate, even to eliminate hazardous effects of Al corrosion.

With good wear resistance, intrinsic wettability, chemical stability, and biocompatibility, alumina ceramics have been widely used as orthopedic implant materials, especially as dental and bone replacement [8-10]. However, like most of the ceramic materials, alumina ceramics have intrinsically poor elasticity and bear a high risk of fracture [11]. In recent studies, alumina ceramics have been used as coatings in conjunction with metallic substrates for biomedical use [12-15]. The ceramic provides the hardness and wear resistance while the metallic component provides toughness and high strength for load bearing applications [16]. Therefore, to combine the advantages of aluminum and alumina, we designed and fabricated an Al_2O_3-coated aluminum alloy with a ceramic-on-metal structure. By using micro-arc oxidation (MAO) [17-19], a thick and double-layer structured Al_2O_3 coating can be grown *in-situ* on aluminum alloy [20]. The dense inner layer of the Al_2O_3 coating with high bonding strength to the substrate can protect the underlying Al alloys from the external environment and prevent the exfiltration of toxic Al ions. In addition, by mimicking the micro-structure of natural bones, the porous outer layer of the Al_2O_3 coating can facilitate bone growth *in vitro* and *in vivo*. Moreover, in this work, specific biologically important elements, such as Zn, Ca, and Fe, are incorporated into the Al_2O_3 coatings *in situ* to obtain the favorable biological functions by MAO in special modified electrolyte. The samples with and without the Al_2O_3 coatings are systematically characterized and *in vitro* experiments are performed to investigate the osteogenic and antibacterial capabilities.

2. Materials and methods

2.1. Sample Preparation

MAO was used to produce coatings with different doping elements on the LY12 Al alloy. Before MAO, the substrate was polished with SiC abrasive paper, degreased, and rinsed with acetone and distilled water. MAO was conducted in the corresponding electrolytes composed of the primary salt of sodium hexametaphosphate ($(NaPO_3)_6$, 15-20 g/L, XiLong Science Co., Ltd) and other additives at a constant current density (5 A/dm^2) at 500 Hz for 8 min with a duty cycle of 12% and 20 kW AC power supply (Chengdu JINCHUANGLI Technology Co., Ltd, JCL-WH20). In order to incorporate Ca, Fe and Zn, calcium acetate hydrate ($C_4H_6CaO_4 \cdot H_2O$, 3 g/L, XiLong Science Co., Ltd), ammonium iron (III) oxalate hydrate ($C_6H_{12}FeN_3O_{12} \cdot 3H_2O$, 6 g/L, XiLong Science Co., Ltd), or zinc acetate hydrate ($C_4H_6O_4Zn \cdot 2H_2O$, 5 g/L, XiLong Science Co., Ltd) were introduced to the electrolyte, respectively. The undoped sample served as the control for comparison. During MAO, the temperature of the electrolyte was controlled to be below 40 ºC with an external water cooling system. After the surface treatment, the samples were cut to the required dimensions by a simple cutting machine, rinsed with distilled water, and dried.

2.2. Sample Characterizations

The structure of the samples was analyzed by X-ray diffraction (XRD, Bruker, D8 Advance) equipped with an X-ray source of Cu target (λ = 0.15418 nm). The data

were collected at 2θ = 10°~80° at a scanning rate of 2θ = 5°/min. The samples were analyzed by X-ray photoelectron spectroscopy (XPS, ESCALAB 250X, Thermo Fisher) referenced to the C1s peak (284.8 eV). The energy of Al K_α irradiation at the sample surface is 1486.6 eV. The surface morphology was examined by field-emission scanning electron microscopy (FE-SEM, Carl Zeiss, SUPRA® 55) and the elemental composition and lateral distribution were determined by energy-dispersive X-ray spectroscopy (EDS). To assess the corrosion behavior, polarization curves were acquired on an electrochemical workstation (1470E, Solartron Metrology) between -2.0 and 0 V versus the saturated calomel electrode (SCE) at a scanning rate of 10 mV/s at 25 ºC in the NaCl (3.5 wt%) and simulated body fluid (SBF) solutions, respectively. The corrosion potential (E_{corr}) and corrosion current density (i_{corr}) were analyzed by the Tafel extrapolation method. Scratch tests were measured on a scratch tester (WS-2005, Lanzhou Institute of Chemical Physics, Chinese Academy of Sciences). In the test, the load on a diamond indenter with an included angle of 120° was linearly increased from 0 to 100 N at a rate of 20 N/min at 25 ºC and 65±1% RH. The wear resistance was evaluated on a friction-wear tester (MFT-5000, Rtec Instrument) at 25 ºC and 65±1%RH. GCr15 steel balls with diameter of 4 mm, surface roughness of 0.02 μm and hardness of 64 HRC were used as the counterpart materials. All wear tests were conducted with GCr15 steel balls that slide against the middle of MAO coatings in a circular motion with a radius of 5 mm. The rotating speed and normal load of the wear tester were 200 r/min and 3 N, respectively. The depth profiles and topographies of the wear track were detected

using a VK-X200 laser confocal microscope. The surface contact angles were measured on contact angle meter (PT-705B, Dong Guan Precise Test Equipment CO.; LTD) at 25 ºC and 55 ± 1% RH. For statistical accountability, more than 6 measurements were performed on each sample and the average values were calculated. The thickness of the MAO coatings was determined on an eddy current thickness meter (CTY2300, SDCH. Co.; LTD) and multiple measurements were conducted to obtain averages. The simulated body fluid (SBF) was used as the culture medium in the immersion experiments at 37 ºC and inductively-coupled plasma atomic emission spectrometry (ICP-AES, JY2000-2, Horiba) was employed to monitor the time-dependent dissolution of Al ions from the samples. The volume of SBF was calculated by the following equation [21]: $V_s = S_a / 10$, where V_s is the volume of SBF (mL) and S_a is the apparent surface area of each sample (mm^2).

2.3. Cell Culture

The human bone mesenchymal stem cells (hBMSCs) were obtained from ATCC and maintained in the culture medium composed of the α-minimum essential medium (α-MEM, Hyclone), 10% fetal bovine serum (FBS, Corning), and 1% penicillin/streptomycin (Invitrogen). After expanding to passage 5, the hBMSCs were seeded onto the samples with different dimensions and cultured. Before cell seeding, the samples were sterilized with 75% ethanol overnight and rinsed with the sterile phosphate-buffered saline (PBS) solution. The cultures were incubated in a humidified atmosphere of 5% CO_2 at 37 ºC and the culture medium was refreshed

every 3 days.

2.3.1. *Cell viability*

The hBMSCs were seeded onto 10 mm × 10 mm samples (1×10^4 cells per sample) on 24-well tissue culture plates. After culturing for 1, 3, and 7 days, the cells were quantitatively investigated with the cell viability assay using the CCK-8 kit (Donjindo). At each time point, the harvested specimens were rinsed thrice with PBS and incubated with the 10% CCK-8 reagent in the culture medium (0.7 ml) for 4 hours. Afterwards, 100 μl of the incubated mixture was transferred to a 96-well plate and analyzed spectrophotometrically at 450 nm (Multiskan GO, Thermo Fisher).

2.3.2. *Live/dead staining*

Live/Dead Cell staining was performed on the 10 mm × 10 mm samples on 24-well plates were seeded with the hBMSCs at a density of 1×10^4 cells per sample. After culturing for 3 days, the cells were rinsed thrice with PBS, stained for 15 min in darkness with the Live/Dead Cell Staining Kit (BioVision), and examined by fluorescence microscopy (Olympus BX53).

2.3.3. *Flow Cytometry*

Apoptosis and necrosis of the hBMSCs on the samples were evaluated with the Annexin V-FITC/PI assay (TransStart) according to the manufacturer's instructions. Briefly, the hBMSCs were cultured for 3 days, harvested, rinsed with PBS, and

stained with Annexin V-FITC and PI. The apoptotic cells labeled with Annexin V-FITC and necrotic cells labeled with PI were analyzed on a cell Lab Quanta SC flow cytometry instrument (Beckman coulter).

2.3.4. *Cell morphology*

After incubation for 3 days, the cells on the samples were rinsed thrice with PBS and fixed with 2.5% glutaraldehyde for 15 min. Prior to FE-SEM (Carl Zeiss, SUPRA® 55), the specimens were sequentially dehydrated in gradient ethanol solutions (30, 50, 75, 90, 95 and 100 v/v %) for 15 min and final dehydration was conducted in hexamethyldisilazane. Afterwards, the samples were dried, sputter-coated with platinum, and examined by FE-SEM.

2.3.5. *Quantitative real-time PCR*

The osteogenesis-related gene expressions of the hBMSCs on the samples were quantitatively analyzed by the real-time polymerase chain reaction (real-time PCR). Samples with a dimension of 20 mm × 20 mm were seeded with hBMSCs at a density of 5×10^4 cells per sample on 6-well plates. The cells were cultured in a basic growth medium initially for 3 days and the osteogenic medium (basic medium with 5 μmol/ml glycerophosphate, 50 μg/ml ascorbic acid, and 100 pmol/ml dexamethasone) was refreshed for subsequent incubation.

After osteogenic induction for 3, 7, and 14 days, the total RNA of the cultured cells was extracted by using the Trizol reagent (Life Technologies) and 2 μg of total

RNA from each specimen was reversely transcribed into cDNA by using a RevertAid First Strand cDNA Synthesis Kit (Thermo Scientific) according to the manufacturer's instructions. RT-PCR was performed on a real-time PCR system (BIO-RAD) to analyze the gene expressions of alkaline phosphatase (ALP), bone sialoprotein (BSP), and osteocalcin (OCN) with β-actin serving as the endogenous gene for normalization. The primer sequences are listed in Table 1 and quantification of the gene expressions was based on the comparative cycle-threshold (C_T) method expressed as $2^{-\Delta\Delta C_T \pm SD}$[22].

2.3.6. *Mineralization Assay*

Mineralization of the hBMSCs was assessed by Alizarin Red staining. Samples with dimensions of 20 mm × 20 mm were seeded with hBMSCs at a density of 5×10^4 cells per sample on 6-well plates. The cells were cultured in a basic growth medium initially for 3 days and then the osteogenic medium (basic medium with 5 μmol/ml glycerophosphate, 50 μg/ml ascorbic acid, and 100 pmol/ml dexamethasone) was refreshed for subsequent incubation. After osteogenic induction for 21 days, the cells were rinsed thrice with PBS, fixed with 95% alcohol for 10 min, and rinsed with distilled water three times. The specimens were then stained with 40 mM Alizarin Red (pH 4.2, Sigma), dissolved in 10% cetyl pyridinium chloride (Sigma), and analyzed for extracellular matrix (ECM) mineralization spectrophotometrically at 540 nm (Multiskan GO, Thermo Fisher).

2.4. *Antibacterial tests*

The antibacterial properties were determined by the plate-counting method with Gram-positive *Staphylococcus aureus* (*S. aureus*, ATCC 25923) and Gram-negative *Escherichia coli* (*E. coli*, ATCC 25922) as the bacteria models. Both bacteria were cultivated in the beef extract-peptone (BEP) at 37 ºC and adjusted to a concentration of 5×10^5 CFU/ml. 400 μl of the bacterial suspension was added to each sample (50 mm × 50 mm) which was then covered with a polyethylene membrane (40 mm × 40 mm). After 24 hours, the samples were washed with sterile PBS. The PBS eluents were diluted 10^5 times and laid on Luriae-Bertani (LB) agar plates for another 24 hours. The active bacteria were counted according to the National Standard of China ISO-22196-2011 protocol and the antibacterial ratio was calculated using the following formula:

$$\frac{\left(\bar{C}-\bar{T}\right)}{\bar{C}}\times100\%,$$

where $\bar{C}$ was the average number of bacteria on pristine Al alloy substrate (CFU/sample) and $\bar{T}$ was the average number of bacteria on the various MAO samples (CFU/sample).

2.5. Statistical analysis

The *in vitro* assays were performed in triplicate and each value was expressed as mean ± standard deviation. Each *in vitro* experiment was repeated three times with the typical data shown. Statistical evaluation was performed by one-way ANOVA, where $p < 0.05$ was considered significant and $p < 0.01$ was considered highly significant.

3. Results

3.1. Surface characterizations

Fig. 1 shows the surface morphology of the samples and volcano-like porous structures are observed. The pore size varies from several nanometers to more than ten micrometers. In particular, the surface of the Fe-doped sample has the least amount of pores and smallest average pore size but the undoped and Zn-doped samples show more pores. According to EDS results, the coatings are mainly composed of Al, P, and O. Besides, Ca, Fe, and Zn are also detected from the corresponding doped coatings, respectively. The surface wettability is indicated by the typical water droplet images shown on the top-right in Fig. 1. The Ca, Zn, and Fe-doped samples show a similar water contact angle of about 35° whereas the water contact angle of the undoped sample is 55°. The Al_2O_3 coatings formed on the Al alloy are mainly composed of Al, P, and O in the phosphate electrolyte [23] in addition to the respective dopant element (Ca, Fe, or Zn).

Generally, the micro-arc oxidation coatings have the double-layer structure [20, 24]. Fig. 2 shows both outer and inner layers in the Zn-doped sample. As shown in Fig. 2A, the loose and volcano-like porous structure exists in the outer MAO layer, which is formed by the liquid plasma containing molten Al and alumina during the breakdown of the weakest location repeatedly under the electric field [25, 26]. Compared to the porous outer layer, the inner layer (Fig. 2B) in the coating is much more compact with few pores. The inner layer in the Zn-doped sample has a thickness

of about 3 μm and is abundant with Al, O, and P (Fig. 2C, 2D, and Fig. S2 in supporting information), whereas more Zn is detected from the outer layer. The results of other Al_2O_3 samples are presented in Figs. S3-S5 and the similar results are observed. All the Al_2O_3 coatings have similar thicknesses with an outer layer thickness of 10 to 15 μm and an inner layer thickness of 3 to 5 μm (Fig. S6). Contrary to the loose structure of the outer layer, the compact structure of inner MAO layer, which enhances the anti-corrosion performance and inhibits release of Al ions from the Al alloy substrate, is formed in the last stage of the MAO process [27].

Fig. 3A shows the crystal phases determined by XRD and the pristine Al alloy substrate serves as the control. The Al_2O_3 samples show typical peaks of γ-Al_2O_3 and α-Al_2O_3 arising from the Al alloy substrate. Since the instantaneous temperature in a small arc discharge region is over 2000 ºC, the thermodynamically stable α-Al_2O_3 phase can formed in the inner layer [26]. In contrast, the γ-Al_2O_3 phase mostly presents in the outer layer due to fast cooling by the electrolyte [28]. Besides Al_2O_3, no other diffraction peaks of the dopants can be observed, which maybe results from the small concentration and amorphous state. However, the XPS results shown in Fig. 3B and 3D reveals the presence of Ca, Fe, and Zn with the concentrations of 4.5%, 3.0%, and 1.0%, respectively in the doped samples. The binding energies of Fe, Ca, Zn are 710.2 eV ($Fe2p/_{3/2}$), 348.1 eV ($Ca2p/_{3/2}$), and 1022.5 eV ($Zn3p/_{3/2}$) respectively (Fig. 3C), corresponding to metal oxides or metal phosphates, which indicates the presence of iron, calcium, zinc oxide or phosphate in the films.

3.2. Adhesion, corrosion and wear resistance performance

Acoustic emission produced in the scratch test is utilized to evaluate the interface bonding strength of the Al_2O_3 coatings. Fig. 4A shows that the adhesion strength of all the Al_2O_3 coatings is above 30 N and follows the order of Fe-doping (62.0 N) > Zn-doping (46.3 N) ≈ Ca-doping (46.0 N) > No doping (38.2 N), indicating that the adhesion strength of the Al_2O_3 coating can be improved by doping. As shown in the Fig. S7, the discharge of the Fe-doped sample is more intense compared to those of Ca-doped and Zn-doped samples, which induces the much stronger arc stirring at the interface between the coating and Al substrate. Therefore, the Fe-doped sample exhibits the largest adhesion. The improved adhesion between the MAO coating and substrate mitigates the risk of aseptic loosening caused by delamination of the coating [29].

Fig. 4B shows the dynamicpotential polarization curves of pristine Al alloy substrate and Al_2O_3 samples measured in 3.5 wt% NaCl solution. The i_{corr}, E_{corr}, and β_c values are calculated by Tafel extrapolation from the linear cathodic polarization region and the results are shown in Table. 2. The pristine Al alloy exhibits the worst anti-corrosion behavior with the smallest corrosion potential and largest corrosion current density. After MAO treatment, E_{corr} increases and i_{corr} decreases obviously, demonstrating a significant enhancement in the corrosion resistance. Similar results are also obtained from the polarization test in the SBF solution (Fig. S8 and Table S1). It has been reported that the dense inner layer can prevent penetration of the solution to the underlying substrate leading to well corrosion resistance [30]. Besides, the

corrosion resistance depends on the structure of the MAO coatings[31]. On account of the least pores and the smallest average pore size, the Fe-doped sample shows the best anti-corrosion performance.

Fig. 4C, 4D, and Fig. S9 show the friction and wear behavior of different samples. Compared to the Al alloy substrate with the friction coefficient of about 1.0 and the wear depth of about 15 μm only after 77 turns, the wear resistances of all the Al_2O_3-coated samples increase. Especially, the Zn-doped sample possesses the smallest friction coefficient of about 0.5 and which further decreases to about 0.3 with increasing wear time. No apparent wear scratch can be observed on all the Al_2O_3-coated samples after 12,000 turns, while Ti6Al4V shows a deep wear scar more than 30 μm after 12,000 turns due to its lower hardness than GCr15 steel ball, although its friction coefficient is as good as the Al_2O_3-coated samples (Fig. 4D). The Al_2O_3 coatings can improve the wear resistance of the Al alloy thereby prolonging the service lifetime and lowering inflammation risks caused by released particles [32].

3.3. In-vitro biocompatibility

Al leaching tests are conducted to evaluate the protection effects of the Al_2O_3 coatings. As shown in Fig. 5A, leaching of Al^{3+} ions from the pristine Al alloy substrate increases from 0 mg/L to over 80 mg/L after immersion for 28 days. However, after the same immersion time, the amount of the Al ions releasing from the Al_2O_3-coated samples is below 0.2 mg/L, even lower than that dissolves from Ti6Al4V, which can be ignored considering the test error. Besides, according to the

World Health Organization, daily ingestion of aluminum of 0~0.6 mg/kg is biosafe to human being. In this work, the dosage of Al ions leaching out has been greatly reduced to a concentration below the toxicity criterion by MAO treatment. Fig. S10 shows that volcano-like porous structures are observed on the coating surfaces and least and smallest pores occur on the Fe doped sample. The coatings are mainly composed of Al, P, and O and Ca, Fe, and Zn are detected from the corresponding samples. All the results show that no significant change can be found on the surface morphology and chemical compositions after immersion in SBF for 28 days.

For further evaluate the cell cytotoxicity of different samples, hBMSCs are seeded and the CCK-8 assay is employed to measure the time-dependent cell viability after incubation for 1, 3, and 7 days. As shown in Fig. 5B, the Fe-doped sample shows the most positive proliferation of hBMSCs and the other Al_2O_3-coated samples show similar cell viability with the Al alloy substrate and Ti6Al4V in the first day. When the incubation time increases to 3 and 7 days, the difference between the Fe-doped sample and other samples becomes statistically significant. The Fluorescence microscopy and FE-SEM results are presented in Fig. 5C and Fig. S11, and the viable and dead hBMSCs are stained green and red, respectively. All the samples show good cell viability and the cells spread well. Flow cytometry is further performed and reveals that the samples have good cytocompatibility showing low cell apoptosis and necrosis (insets in Fig. 5C). Among them, the Fe-doped sample shows the best performance of cell viability, which can be probably due to the enhanced metabolic activity of cells at an appropriate iron concentration [33].

3.4. In-vitro osteogenesis ability

Osteogenesis of cultured hBMSCs is another crucial factor to the success of bone implants. After culturing for 3, 7, and 14 days, osteogenic induction of the hBMSCs is evaluated by real-time PCR utilizing the primers for bone markers as ALP [34], BSP [35], and OCN[36]. As shown in Figures 6A-6C, the Zn-doped sample is superior exhibiting up-regulation of all the three osteogenic genes. After 14 days, the ALP, BSP, and OCN gene levels observed from the Zn-doped samples are about 2.9, 3.4 and 2.0 times of those of the Al alloy substrate and 2.4, 2.8 and 1.6 times of those of Ti6Al4V, respectively. After 21 days, the hBMSCs are examined by Alizarin Red staining and spectrophotometry. Figure 6D indicates that ECM mineralization of hBMSCs on the Zn-doped sample is the highest. Both gene determination and mineralization assay verify that Zn-doped sample is more desirable from the perspective of osteogenesis. Besides, the other Al_2O_3-coated samples also show varying degrees of improving osteogenesis properties compared with the uncoated Al alloy and Ti6Al4V materials, demonstrating the important and distinguished effect of Al_2O_3 coatings on osteogenesis.

3.5. In-vitro antibacterial ability

In this work, both *S. aureus* and *E.coli* are used to assess the antibacterial ability with bacteria counting and the results are shown in Fig. 7. Compared to the Al alloy substrate and Ti6Al4V, the Al_2O_3-coated samples show less re-cultivated bacterial

colonies after 24 hours for both *E. coli* and *S. aureus*. In particular, the Zn-doped and Fe-doped samples show significant antibacterial efficiency comparing to other samples. For the Zn-doped sample, barely visible bacterial colony can be found, indicating excellent antibacterial property. The antibacterial rates of Zn-doped sample are 99.5 ± 0.56% and 98.77 ± 0.52% against Gram-negative *E. coli* and Gram-positive *S. aureus*, respectively, indicating the potential anti-inflammation properties when the Zn-doped sample is implanted into human body.

4. Discussion

A new generation of bio-functional orthopedic implants possessing both osteoinductivity and antibacterial ability and bone modulus by simple and low-costly methods is demanded in clinical applications[37, 38]. As illustrated in Fig. 8, after MAO treatment, a double-layer Al_2O_3 coating is formed on the Al alloy (Fig. 2). On the one hand, the compact inner layer enhances the mechanical and anti-corrosion performance (Fig. 4) and inhibits the release of potentially harmful Al ions from the Al alloy substrate (Fig. 5). On the other hand, the outer layer has a porous rough surface in the micrometer range similar to the micro-structure of natural bones, which generally can facilitate the osteogenic differentiation of osteoblast [39-41]. Therefore, comparing to the untreated Al substrate and the Ti6Al4V sample, not only the doped Al_2O_3 samples, but also the undoped Al_2O_3 sample show better osteogenesis activity (Fig. 6), suggesting the improvement of the osteogenesis is induced by the MAO treatment.

Moreover, Zn, Fe and other elements can be easily doped into the porous outer layer, which also play important roles in the osteoblast proliferation and differentiation in addition to antibacterial processes. As shown in Fig. 6 and Fig. 7, the Zn-doped sample shows the best osteogenic and antibacterial performance. The excellent osteogenic activity and antibacterial ability of Zn-doped sample can be mainly due to the released Zn^{2+} ions. It is believed that Zn ions at an appropriate concentration can promote bone formation and have antibacterial effect on bacteria without introducing undesired side effect [42, 43]. Zn^{2+} can be transported to the bacteria cytosol via the ion channels at the expense of energy consumption [44]. The living condition of the bacteria deteriorate as the bacteria transport more Zn^{2+} ions and a high concentration of Zn^{2+} in the cytosol can be detrimental to bacterial cells [34]. Moreover, appropriate amounts of Zn ions released from the Zn-doped sample can be absorbed by cells, thus facilitate the expression of osteogenic-related genes and stimulate bone growth [45, 46]. In our work, the incorporated Zn element in the MAO-coating can diffuse into the medium matrix and cause biological effects on the adhered cells and bacteria.

Summarily, the good cell compatibility, osteogenesis performance and high antibacterial of the Al_2O_3-coated samples are attributed to the synergistic effect of the double-layer structure of the MAO coatings and the doping elements. As a result, the Zn-doped Al_2O_3 coating delivers the outstanding osteogenesis and antibacterial performance, which make it a promising candidate as bone implants.

5. Conclusion

In this work, Al_2O_3 coatings with good adhesion strength and double-layer structure is fabricated to improve the anti-abrasion and anti-corrosion performance and to avoid the leaching out of toxic Al ions. Biological assessment demonstrates that the Fe-doped Al_2O_3 coating significantly improves the cytocompatibility of Al alloy samples. Moreover, the doped metallic elements show biomedical functions on osteogenesis and anti-bacteria. In particular, the Zn-doped sample shows outstanding osteogenic activity and antibacterial effects. The Al_2O_3-coated aluminum alloys have great potential in the development of novel kinds of bone substitute biomaterials in orthopedics.

Acknowledgements

The authors acknowledge financial support from National Materials Genome Project (No. 2016YFB0700600), National Natural Science Foundation of China (NSFC) (No. 51503220), Youth Innovation Promotion Association of the Chinese Academy of Sciences (No. 2017416), Leading Talents of Guangdong province Program (No. 00201520), Shenzhen Peacock Program (No. KQTD20160301115500545), Hong Kong Research Grants Council (RGC) General Research Funds (GRF) CityU No. 11301215, as well as City University of Hong Kong Applied Research Grant (ARG) No. 9667144.

References

[1] M. Fini, G. Giavaresi, P. Torricelli, V. Borsari, R. Giardino, A. Nicolini, A. Carpi, Osteoporosis and biomaterial osteointegration, Biomedicine & Pharmacotherapy 58 (2004) 487-493.

[2] M. Geetha, A.K. Singh, R. Asokamani, A.K. Gogia, Ti based biomaterials, the ultimate choice for orthopaedic implants – a review, Progress in Materials Science 54 (2009) 397-425.

[3] A. Ataee, Y. Li, D. Fraser, G. Song, C. Wen, Anisotropic Ti-6Al-4V gyroid scaffolds manufactured by electron beam melting (EBM) for bone implant applications, Materials & Design 137 (2018) 345-354.

[4] L. Mathieu, F. Marie-Solenne, B. Cécile, L. Jean-Marc, C.J. Julien, D. Patrick, D. Erick, Biocompatibility of four common orthopedic biomaterials following

neuroelectromyostimulation: an in-vivo study, Journal of Biomedical Materials Research Part B Applied Biomaterials 106 (2018) 1156-1164.

[5] M.P. Staiger, A.M. Pietak, J. Huadmai, G. Dias, Magnesium and its alloys as orthopedic biomaterials: a review, Biomaterials 27 (2006) 1728-1734.

[6] H. Tang, Y. Gao, Preparation and characterization of hydroxyapatite containing coating on AZ31 magnesium alloy by micro-arc oxidation, Journal of Alloys & Compounds 688 (2016) 699-708.

[7] H. Tang, Y. Han, T. Wu, W. Tao, X. Jian, Y. Wu, F. Xu, Synthesis and properties of hydroxyapatite-containing coating on AZ31 magnesium alloy by micro-arc oxidation, Applied Surface Science 400 (2016) 391-404.

[8] S.M. Kurtz, S. Kocagöz, C. Arnholt, R. Huet, M. Ueno, W.L. Walter, Advances in zirconia toughened alumina biomaterials for total joint replacement, Journal of the Mechanical Behavior of Biomedical Materials 31 (2014) 107-116.

[9] S. Affatato, E. Modena, A. Toni, P. Taddei, Retrieval analysis of three generations of Biolox® femoral heads: spectroscopic and SEM characterisation, Journal of the Mechanical Behavior of Biomedical Materials 13 (2012) 118-128.

[10] J. Chevalier, L. Gremillard, Ceramics for medical applications: a picture for the next 20 years, Journal of the European Ceramic Society 29 (2009) 1245-1255.

[11] O. Roualdes, M.E. Duclos, D. Gutknecht, L. Frappart, J. Chevalier, D.J. Hartmann, In vitro and in vivo evaluation of an alumina–zirconia composite for arthroplasty applications, Biomaterials 31 (2010) 2043-2054.

[12] E.S. Lukin, S.V. Tarasova, A.V. Korolev, Application of ceramics based on

aluminum oxide in medicine (a review), Glass & Ceramics, 58 (2001) 105-107.

[13] A.R. Walpole, Z. Xia, C.W. Wilson, J.T. Triffitt, P.R. Wilshaw, A novel nano-porous alumina biomaterial with potential for loading with bioactive materials, Journal of Biomedical Materials Research Part A 90 (2009) 46-54.

[14] J.L. Xu, F. Liu, F.P. Wang, L.C. Zhao, Alumina coating formed on medical NiTi alloy by micro-arc oxidation, Materials Letters 62 (2008) 4112-4114.

[15] F. Di Palma, A. Chamson, M.H. Lafage-Proust, P. Jouffray, O. Sabido, S. Peyroche, L. Vico, A. Rattner, Physiological strains remodel extracellular matrix and cell–cell adhesion in osteoblastic cells cultured on alumina-coated titanium alloy, Biomaterials 25 (2004) 2565-2575.

[16] A.S. Vlasov, T.A. Karabanova, Ceramics and medicine (review), Glass & Ceramics 50 (1993) 398-401.

[17] Q.P. Tran, Y.C. Kuo, J.K. Sun, J.L. He, T.S. Chin, High quality oxide-layers on Al-alloy by micro-arc oxidation using hybrid voltages, Surface & Coatings Technology 303 (2016) 61-67.

[18] A. Kuznetsova, T.D. Burleigh, V. Zhukov, J. Blachere, J.T. Yates, Electrochemical evaluation of a new type of corrosion passivation layer: artificially produced Al_2O_3 films on aluminum, Langmuir 14 (1998) 2502-2507.

[19] Y. Cheng, Z. Peng, X. Wu, J. Cao, P. Skeldon, G.E. Thompson, A comparison of plasma electrolytic oxidation of Ti-6Al-4V and Zircaloy-2 alloys in a silicate-hexametaphosphate electrolyte, Electrochimica Acta, 165 (2015) 301-313.

[20] J.H. Wang, M.H. Du, F.Z. Han, J. Yang, Effects of the ratio of anodic and

cathodic currents on the characteristics of micro-arc oxidation ceramic coatings on Al alloys, Applied Surface Science 292 (2014) 658-664.

[21] T. Kokubo, H. Takadama, How useful is SBF in predicting in vivo bone bioactivity?. Biomaterials 27 (2006) 2907-2915.

[22] K.J. Livak, T.D. Schmittgen, Analysis of relative gene expression data using real-time quantitative PCR and the $2^{-\Delta\Delta CT}$ method, Methods 25 (2001) 402-408.

[23] H. Ma, D. Li, C. Liu, Z. Huang, D. He, Q. Yan, P. Liu, P. Nash, D. Shen, An investigation of $(NaPO_3)_6$ effects and mechanisms during micro-arc oxidation of AZ31 magnesium alloy, Surface & Coatings Technology 266 (2015) 151-159.

[24] T. Wei, F. Yan, J. Tian, Characterization and wear- and corrosion-resistance of microarc oxidation ceramic coatings on aluminum alloy, Journal of Alloys & Compounds 389 (2005) 169-176.

[25] G. Sundararajan, L. Rama Krishna, Mechanisms underlying the formation of thick alumina coatings through the MAO coating technology, Surface & Coatings Technology 167 (2003) 269-277.

[26] W. Xue, Z. Deng, Y. Lai, R. Chen, Analysis of phase distribution for ceramic coatings formed by microarc oxidation on aluminum alloy, Journal of the American Ceramic Society 81 (1998) 1365-1368.

[27] W. Xue, Z. Deng, R. Chen, T. Zhang, Growth regularity of ceramic coatings formed by microarc oxidation on Al–Cu–Mg alloy, Thin Solid Films 372 (2000) 114-117.

[28] R. McPherson, Formation of metastable phases in flame- and plasma-prepared

alumina, Journal of Materials Science 8 (1973) 851-858.

[29] M. Sundfeldt, L.V. Carlsson, C.B. Johansson, P. Thomsen, C. Gretzer, Aseptic loosening, not only a question of wear: a review of different theories, Acta Orthopaedica 77 (2006) 177-197.

[30] T. Arunnellaiappan, N. Kishore Babu, L. Rama Krishna, N. Rameshbabu, Influence of frequency and duty cycle on microstructure of plasma electrolytic oxidized AA7075 and the correlation to its corrosion behavior, Surface & Coatings Technology 280 (2015) 136-147.

[31] S. Ji, Y. Weng, Z. Wu, Z. Ma, X. Tian, R.K.Y. Fu, H. Lin, G. Wu, P.K. Chu, F. Pan, Excellent corrosion resistance of P and Fe modified micro-arc oxidation coating on Al alloy, Journal of Alloys & Compounds 710 (2017) 452-459.

[32] C.H. Lohmann, D.D. Dean, G. Köster, D. Casasola, G.H. Buchhorn, U. Fink, Z. Schwartz, B.D. Boyan, Ceramic and PMMA particles differentially affect osteoblast phenotype, Biomaterials 23 (2002) 1855-1863.

[33] S. Zhu, N. Huang, L. Xu, Y. Zhang, H. Liu, H. Sun, Y. Leng, Biocompatibility of pure iron: in vitro assessment of degradation kinetics and cytotoxicity on endothelial cells, Materials Science & Engineering: C 29 (2009) 1589-1592.

[34] G. Jin, H. Qin, H. Cao, S. Qian, Y. Zhao, X. Peng, X. Zhang, X. Liu, P.K. Chu, Synergistic effects of dual Zn/Ag ion implantation in osteogenic activity and antibacterial ability of titanium, Biomaterials 35 (2014) 7699-7713.

[35] G. Jin, H. Qin, H. Cao, Y. Qiao, Y. Zhao, X. Peng, X. Zhang, X. Liu, P.K. Chu, Zn/Ag micro-galvanic couples formed on titanium and osseointegration effects in the

presence of S. aureus, Biomaterials 65 (2015) 22-31.

[36] Y. Qiao, W. Zhang, P. Tian, F. Meng, H. Zhu, X. Jiang, X. Liu, P.K. Chu, Stimulation of bone growth following zinc incorporation into biomaterials, Biomaterials 35 (2014) 6882-6897.

[37] S.B. Goodman, Z. Yao, M. Keeney, F. Yang, The future of biologic coatings for orthopaedic implants, Biomaterials 34 (2013) 3174-3183.

[38] Y. Zhao, H. Cao, H. Qin, T. Cheng, S. Qian, M. Cheng, X. Peng, J. Wang, Y. Zhang, G. Jin, X. Zhang, X. Liu, P.K. Chu, Balancing the osteogenic and antibacterial properties of titanium by codoping of Mg and Ag: an in vitro and in vivo study, ACS Applied Materials & Interfaces 7 (2015) 17826-17836.

[39] C. Zink, H. Hall, D.M. Brunette, N.D. Spencer, Orthogonal nanometer-micrometer roughness gradients probe morphological influences on cell behavior, Biomaterials 33 (2012) 8055-8061.

[40] P.Y. Wang, L.R. Clements, H. Thissen, A. Jane, W.-B. Tsai, N.H. Voelcker, Screening mesenchymal stem cell attachment and differentiation on porous silicon gradients, Advanced Functional Materials 22 (2012) 3414-3423.

[41] A.B. Faia-Torres, S. Guimond-Lischer, M. Rottmar, M. Charnley, T. Goren, K. Maniura-Weber, N.D. Spencer, R.L. Reis, M. Textor, N.M. Neves, Differential regulation of osteogenic differentiation of stem cells on surface roughness gradients, Biomaterials 35 (2014) 9023-9032.

[42] S. Miao, K. Cheng, W. Weng, P. Du, G. Shen, G. Han, W. Yan, S. Zhang, Fabrication and evaluation of Zn containing fluoridated hydroxyapatite layer with Zn

release ability, Acta Biomaterialia 4 (2008) 441-446.

[43] G. Jin, H. Cao, Y. Qiao, F. Meng, H. Zhu, X. Liu, Osteogenic activity and antibacterial effect of zinc ion implanted titanium, Colloids & Surfaces B: Biointerfaces 117 (2014) 158-165.

[44] C.E. Outten, T.V. O'Halloran, Femtomolar sensitivity of metalloregulatory proteins controlling zinc homeostasis, Science 292 (2001) 2488-2492.

[45] H. Zreiqat, Y. Ramaswamy, C. Wu, A. Paschalidis, Z. Lu, B. James, O. Birke, M. McDonald, D. Little, C.R. Dunstan, The incorporation of strontium and zinc into a calcium–silicon ceramic for bone tissue engineering, Biomaterials 31 (2010) 3175-3184.

[46] Y. Ramaswamy, C. Wu, H. Zhou, H. Zreiqat, Biological response of human bone cells to zinc-modified Ca–Si-based ceramics, Acta Biomaterialia 4 (2008) 1487-1497.

Figure captions:

Fig. 1. SEM images and EDS spectra of the MAO samples: (A) Undoped, (B) Ca-doped, (C) Fe-doped, and (D) Zn-doped. For each sample, the typical water droplet image is shown on the top-right.

Fig. 2. SEM images and EDS maps of the Zn-doped sample: (A) SEM images of the inner layer and outer layer of the Zn-doped MAO coating; (B) High-resolution SEM image showing the inner layer of the Zn-doped MAO coating; (C_1-C_4) Corresponding elemental maps of Al, O, Zn and P of the inner layer and outer layer of the coating; (D) Cross-sectional SEM image and EDS maps of the Zn-doped MAO coating.

Fig. 3. XRD and XPS results of the Al alloy substrate and MAO samples: (A) XRD patterns; (B) XPS survey; (C) Fe 2p, Ca 2p, and Zn 3p spectra of the corresponding doped coatings; (D) Atomic percent of the doping elements.

Fig. 4. Adhesion, anti-corrosion and wear resistance performance of different samples: (A) Acoustic emission scratching of various coatings; (B) Potentiodynamic polarization curves of the Al alloy substrate and MAO samples in the NaCl (3.5 wt%) solution; (C) Friction coefficients and (D) Depth profiles of the wear scars on the Al alloy substrate, undoped, Ca-doped, Fe-doped, Zn-doped samples, and Ti6Al4V.

Fig. 5. (A) Time-dependent release of Al^{3+} from the samples after immersion in SBF for 28 days with the inset showing the magnification of the area marked by the blue dashed line; (B) Viability of hBMSCs cultured on the samples for 1, 3 and 7 days and the statistical evaluation performed by comparing the samples with the Al alloy substrate; (C) Live/dead staining assay and flow cytometry analysis (top-right inserts)

of hBMSCs cultured on different samples for 3 days.

Fig. 6. Osteogenic differentiation of hBMSCs on the various samples and real-time PCR analysis of osteogenesis-related genes: (A) ALP, (B) BSP, (C) OCN after osteogenic culturing for 3, 7, and 14 days; (D) Mineralization Assay after osteogenic culturing for 3 weeks. The statistical evaluation is performed by comparing the samples with the Al alloy substrate.

Fig. 7. Antibacterial performance: (A) Re-cultivated bacterial colonies of *E. coli* and *S. aureus* on the samples after incubation for 24 hours; Antibacterial efficiency against (B) *E. coli* and (C) *S. aureus*. The statistical evaluation is performed by comparing the samples with the Al alloy substrate.

Fig. 8. Schematic diagram of MAO coating inhibiting release of Al ions and enhancing biological properties after doping.

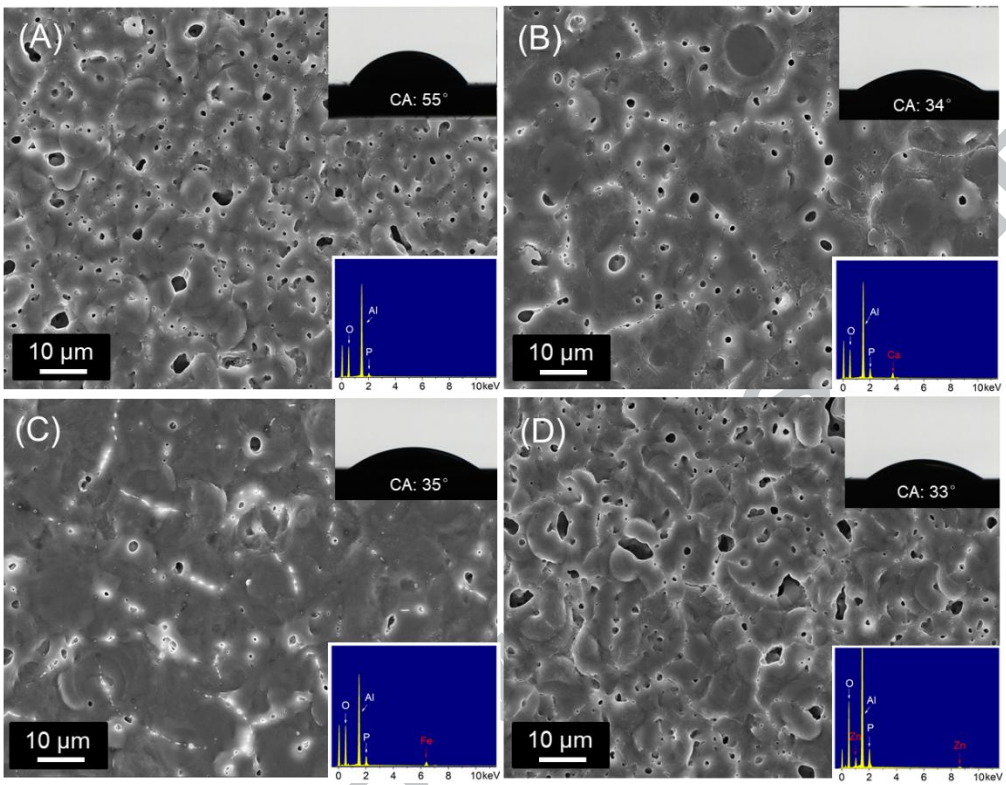

Fig. 1 SEM images and EDS spectra of the MAO samples: (A) Undoped, (B) Ca-doped, (C) Fe-doped, and (D) Zn-doped. For each sample, the typical water droplet image is shown on the top-right.

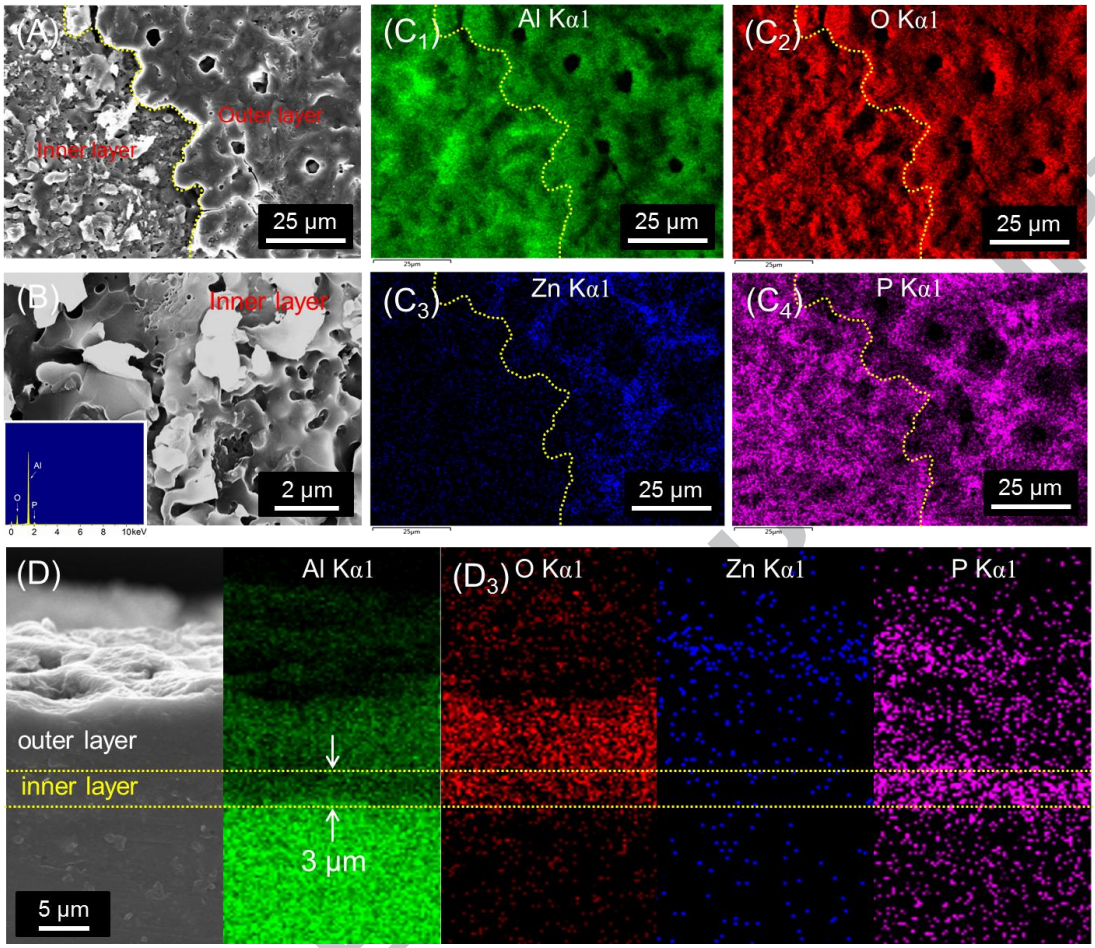

Fig. 2. SEM images and EDS maps of the Zn-doped sample: (A) SEM images of the inner layer and outer layer of the Zn-doped MAO coating; (B) High-resolution SEM image showing the inner layer of the Zn-doped MAO coating; (C_1-C_4) Corresponding elemental maps of Al, O, Zn and P of the inner layer and outer layer of the coating; (D) Cross-sectional SEM image and EDS maps of the Zn-doped MAO coating.

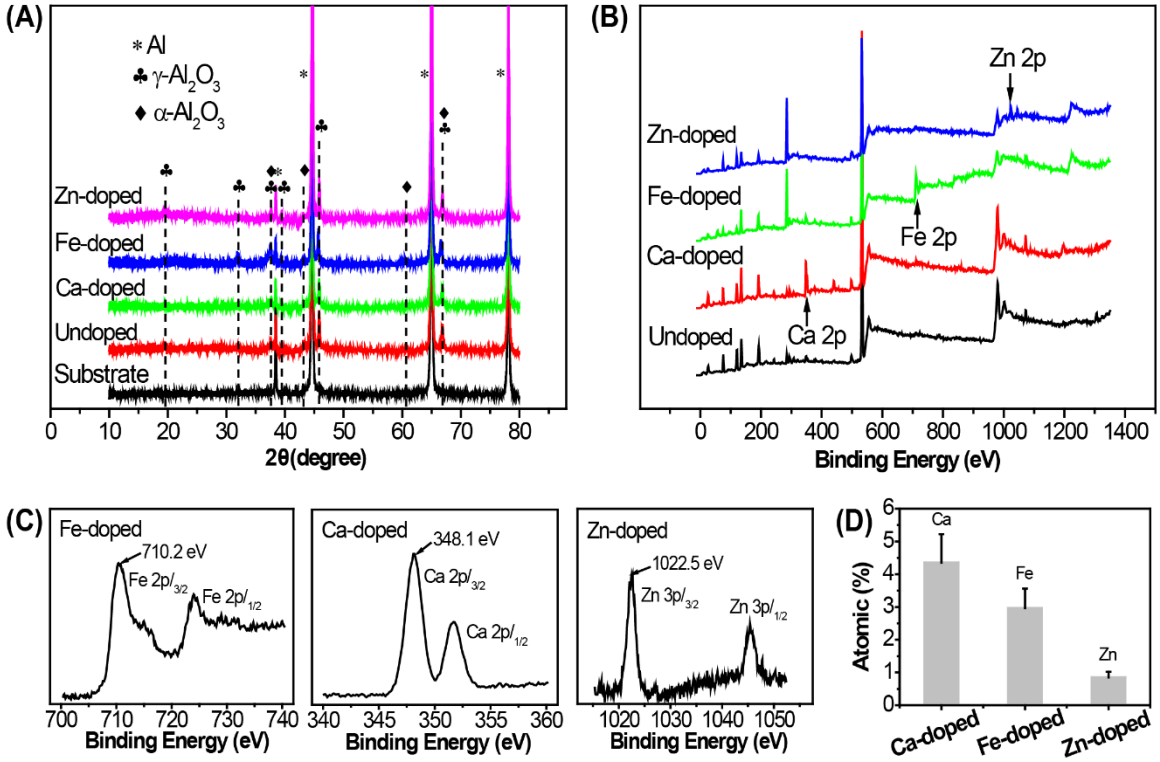

Fig. 3. XRD and XPS results of the Al alloy substrate and MAO samples: (A) XRD patterns; (B) XPS survey; (C) Fe 2p, Ca 2p, and Zn 3p spectra of the corresponding doped coatings; (D) Atomic percent of the doping elements.

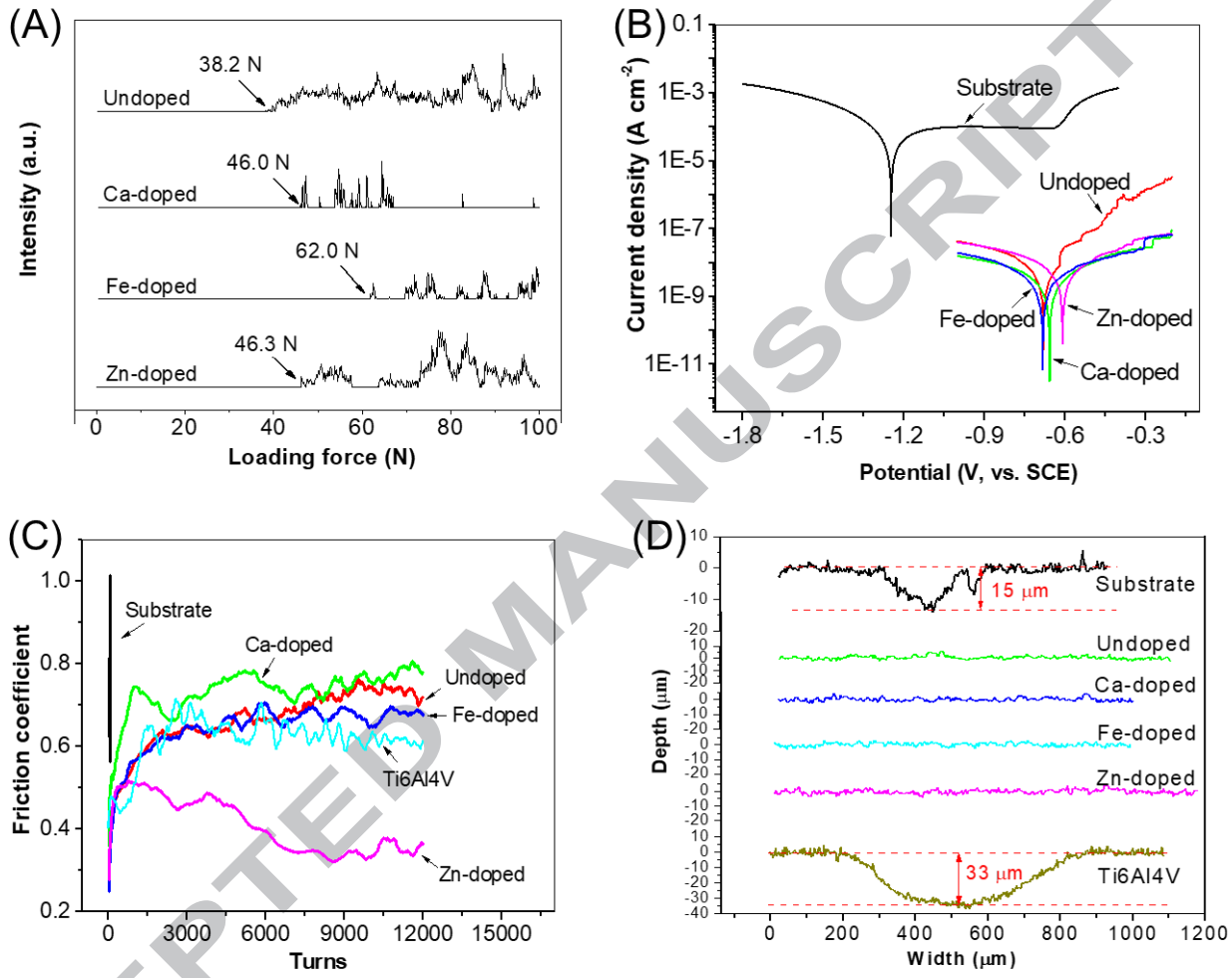

Fig. 4. Adhesion, anti-corrosion and wear resistance performance of different samples: (A) Acoustic emission scratching of various coatings; (B) Potentiodynamic polarization curves of the Al alloy substrate and MAO samples in the NaCl (3.5 wt%) solution; (C) Friction coefficients and (D) Depth profiles of the wear scars on the Al alloy substrate, undoped, Ca-doped, Fe-doped, Zn-doped samples, and Ti6Al4V.

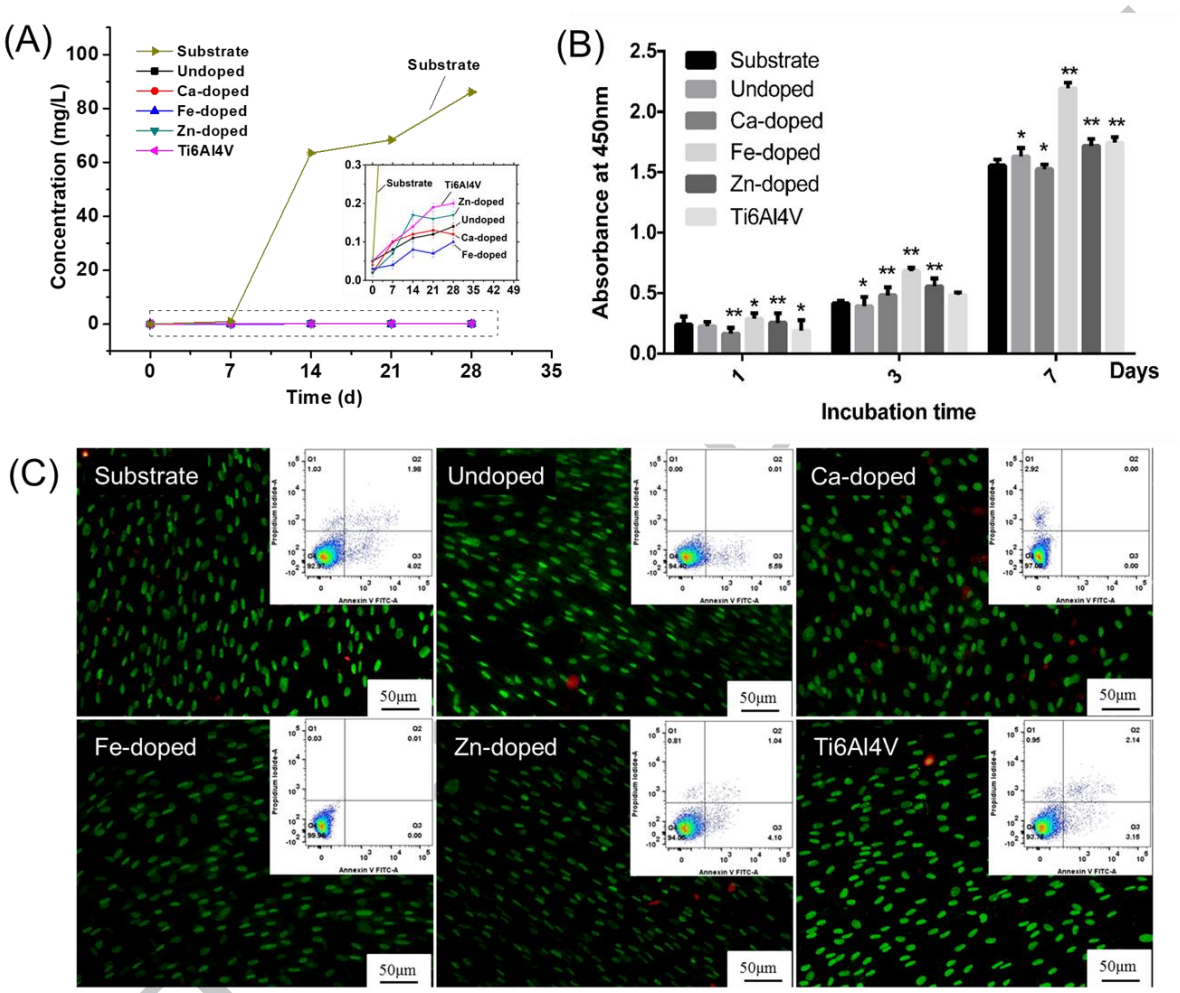

Fig. 5. (A) Time-dependent release of Al^{3+} from the samples after immersion in SBF for 28 days with the inset showing the magnification of the area marked by the blue dashed line; (B) Viability of hBMSCs cultured on the samples for 1, 3 and 7 days and the statistical evaluation performed by comparing the samples with the Al alloy substrate; (C) Live/dead staining assay and flow cytometry analysis (top-right inserts) of hBMSCs cultured on different samples for 3 days.

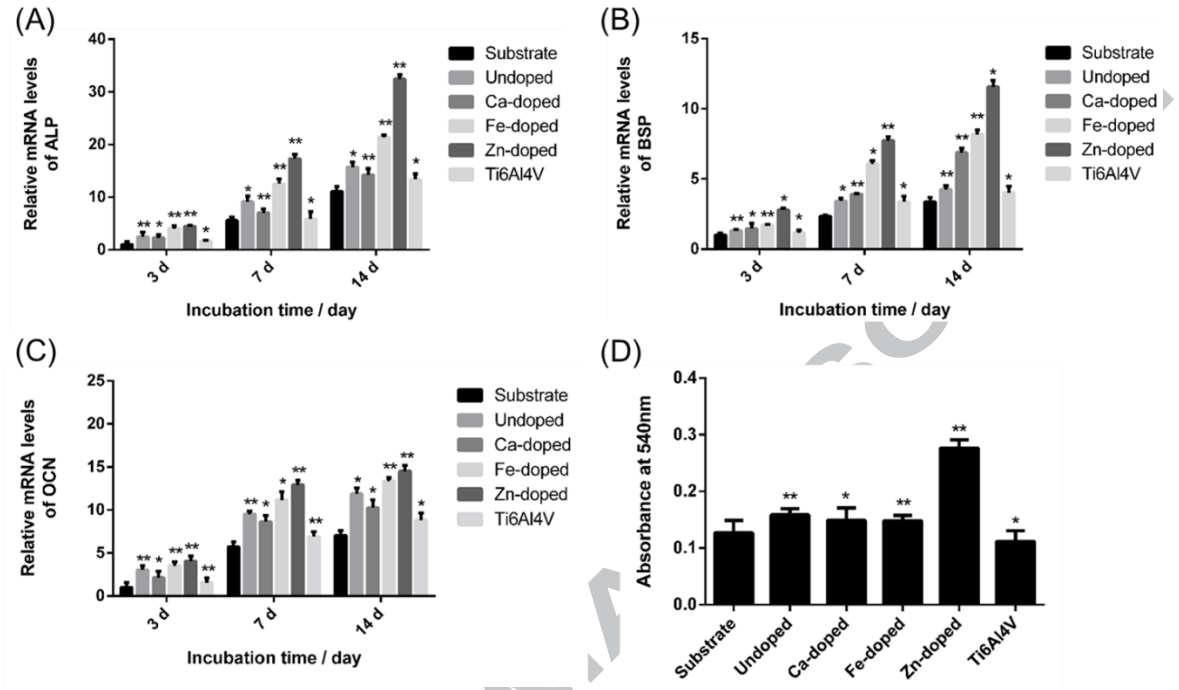

Fig. 6. Osteogenic differentiation of hBMSCs on the various samples and real-time PCR analysis of osteogenesis-related genes: (A) ALP, (B) BSP, (C) OCN after osteogenic culturing for 3, 7, and 14 days; (D) Mineralization Assay after osteogenic culturing for 3 weeks. The statistical evaluation is performed by comparing the samples with the Al alloy substrate.

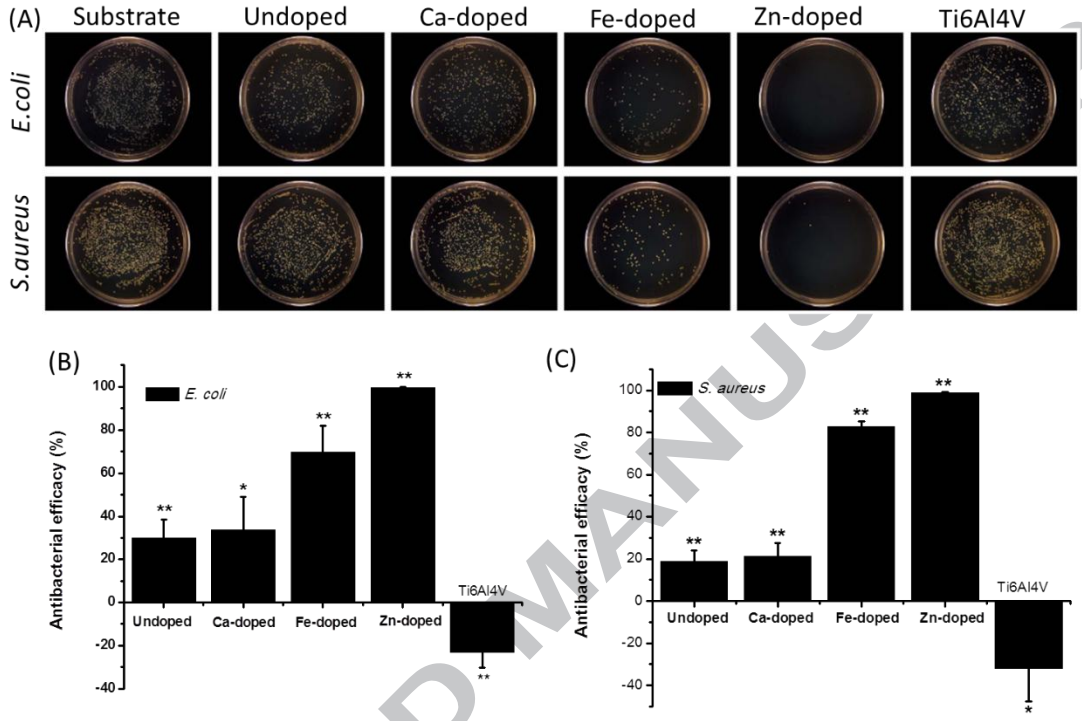

Fig. 7. Antibacterial performance: (A) Re-cultivated bacterial colonies of *E. coli* and *S. aureus* on the samples after incubation for 24 hours; Antibacterial efficiency against (B) *E. coli* and (C) *S. aureus*. The statistical evaluation is performed by comparing the samples with the Al alloy substrate.

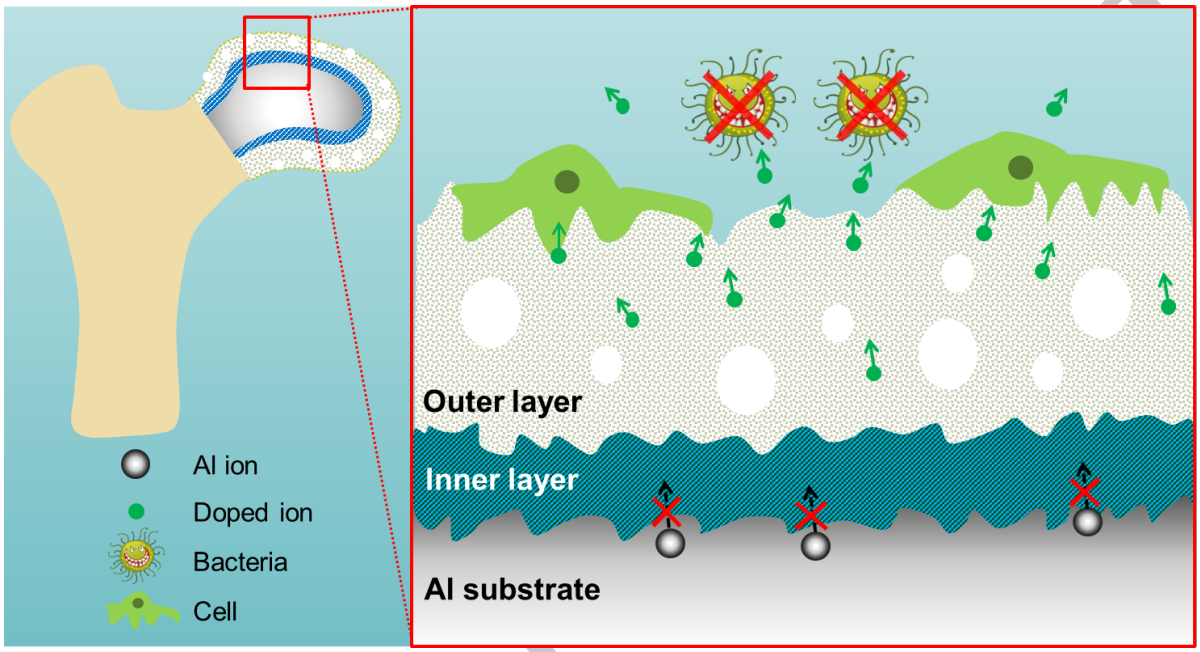

Fig. 8. Schematic diagram of MAO coating inhibiting release of Al ions and enhancing biological properties after doping.

Table 1. Primer sequences used in real-time PCR.

Gene	Forward primers	Reverse primers
ALP	CCCAAAGGCTTCTTCTTG	CTGGTAGTTGTTGTGAGC
BSP	CTTGGAAGGGTCTGTGGGG	TTGACGCCCGTGTATTCGTAC
OCN	GCCTTTGTGTCCAAGC	GGACCCCACATCCATAG
β-actin	TGGCACCCAGCACAATGAA	CTAAGTCATAGTCCGCCTAG

Table 2. Electrochemical corrosion parameters measured in 3.5 *w*t% NaCl solution from the untreated aluminum alloy and MAO coatings prepared with different doping elements after stabilizing for 1 h at the open circuit potential: corrosion current density (i_{corr}), corrosion potential (E_{corr}), and cathodic Tafel slopes (β_c).

Samples	NaCl (3.5 *w*t%)		
	i_{corro} (A cm^{-2})	E_{corro} (V, vs. SCE)	β_c (V dec^{-1})
Substrate	1.22*10^{-4}	-1.25	0.160
Undoped	1.18*10^{-8}	-0.68	0.175
Ca-doped	5.76*10^{-9}	-0.65	0.210
Fe-doped	5.67*10^{-9}	-0.68	0.208
Zn-doped	1.43*10^{-8}	-0.61	0.220

Highlights

- Al_2O_3 coatings are fabricated on Al alloy to improve the wear/corrosion resistance.
- The Al_2O_3 coatings can prevent the release of harmful Al^{3+}.
- The porous outer layer of coating can mimic natural bone to facilitate bone growth.
- The coatings are doped with some metal elements to tune the biological properties.
- The Zn-doped sample shows outstanding osteogenic and antibacterial activity.

Graphical Abstract